Available online at www.sciencedirect.com

SciVerse ScienceDirect

Ceramics International 39 (2013) 5287–5294

CERAMICS INTERNATIONAL

www.elsevier.com/locate/ceramint

Phase transformation characterization of olivine subjected to high temperature in air

Rudy Michel, Mohamed Ramzi Ammar, Jacques Poirier*, Patrick Simon

CEMHTI, CNRS UPR 3079/Université d'Orléans, 1D Avenue de la Recherche Scientifique, 45071 Cedex 2, France

Received 20 September 2012; received in revised form 10 December 2012; accepted 10 December 2012
Available online 22 December 2012

Abstract

Olivine is one of the well-suited materials for fluidized bed reactor technology. After calcination at high temperature, olivine undergoes phase transformations resulting in dehydration and oxidation of fayalite to hematite and magnetite. The transformation mechanisms of olivine subjected to a calcination process at 1400 °C for 4 h are studied. Calcined olivine is characterized by X-Ray Diffraction (XRD), *in situ* XRD at varying temperatures and Raman spectroscopy. This paper explains the contribution of Raman spectroscopy to the study of iron oxide with regard to XRD. The heterogeneous distribution of hematite, magnetite and forsterite in the calcined material is exhibited by Raman mapping.

Keywords: Olivine; Raman spectroscopy; Magnetite; Hematite

1. Introduction

Biomass gasification is a complex thermochemical process that consists the reaction of the fuel with the gasifying agent, in 750–900 °C temperature range, to form energetic gases such as hydrogen, carbon monoxide, carbon dioxide and methane. All these gases are produced together with vapors which condense under ambient conditions and are collectively known as tar, and a solid residue consisting of char and ash [1].

Among the biomass gasification technologies, the bubbling fluidized bed (BFB) is considered as the best adapted reactor operating in 1–12 MWe power range. The bed is maintained in a fluidized state by the gasifying medium and allows achieving an homogeneous temperature distribution (750–900 °C) and an adequate mixing of material in the BFB reactor [2]. The resulting homogeneous temperature distribution is one of the important advantages of the fluidized bed over other reactor concepts [3], as well as their flexibility for a variety of fuels [3,4].

Olivine $(Mg,Fe)_2SiO_4$ is usually used as a bed material in the gasification process, due to its catalytic effect and efficiency of tar decomposition [2]. It is one of the abundant minerals in the earth crust, consisting of a natural solid-solution of magnesium silicate (forsterite Mg_2SiO_4) and iron silicate (fayalite Fe_2SiO_4).

However, fluidized beds have a tendency for agglomeration when they react with biomass ashes, forming new compounds with low melting points (500–1000 °C). This behavior seems to result in molten ash which acts like "glue" between the bed particles [2,5]. Therefore, agglomeration is mainly dependent on the process temperature, where the high temperature greatly affects the agglomeration processes [6–8].

Olivine is not an inert silicate and the resulting phase transformations are not well understood. Only few studies are reported in the literature, with most information reported in the field of earth and environmental science. For instance, Heaton and Engstrom [8] have observed the formation of veins of magnetite and serpentine in fayalite olivine, using *in situ* atomic force microscopy. Mayhew et al. [9] have followed dynamic changes of the oxidation state of iron in environmental systems during progressive fluid–mineral interactions. Swierczynski et al. [10,11] have shown the behavior of olivine in oxidizing–reducing conditions. They have also shown improvement of the

*Corresponding author.
E-mail address: jacques.poirier@univ-orleans.fr (J. Poirier).

0272-8842/$ - see front matter © 2012 Elsevier Ltd and Techna Group S.r.l. All rights reserved.
http://dx.doi.org/10.1016/j.ceramint.2012.12.031

mechanical and catalytic properties of olivine by exposing the material to a temperature of 1400 °C in air for 4 h [11].

The present study aims to provide a comprehensive understanding of the phase transformations of olivine calcined to high temperature (1400 °C) for use in a fluidized bed reactor as a catalyst. Thermodynamic analysis, XRD, and Raman spectroscopy were used to investigate the olivine behavior. This work is also focused on the interest and the applicability of Raman spectroscopy, particularly in its mapping mode.

2. Experimental section

2.1. Olivine as a mineral phase

Olivine M_2SiO_4 (M = Mg, Fe) is an orthosilicate of orthorhombic Pbnm structure (forsterite (M = Mg): a = 0.475, b = 1.020, and c = 0.598 nm; fayalite (M = Fe): a = 0.482, b = 1.048, and c = 0.609 nm) [12].

The structure of olivine consists of isolated SiO_4^{4-} tetrahedra, where each of the tetrahedra oxygen atoms is shared by three octahedral cations. M atoms occupy half of the available octahedral voids, with Si atoms occupying one-eighth of the available voids. The half M atoms (M1 site) are located at symmetry centers ($\bar{1}$) and the remaining ones (M2 site) on reflexion planes (m). Each oxygen atom is bonded to one silicon and three octahedra coordinated atoms [12]. For instance, Fig. 1 displays a view of the crystallographic structure of forsterite Mg_2SiO_4 where the M1 site is labeled Mg1. The Fe^{2+} atom is larger than Mg^{2+} and has a preference for the M1 site.

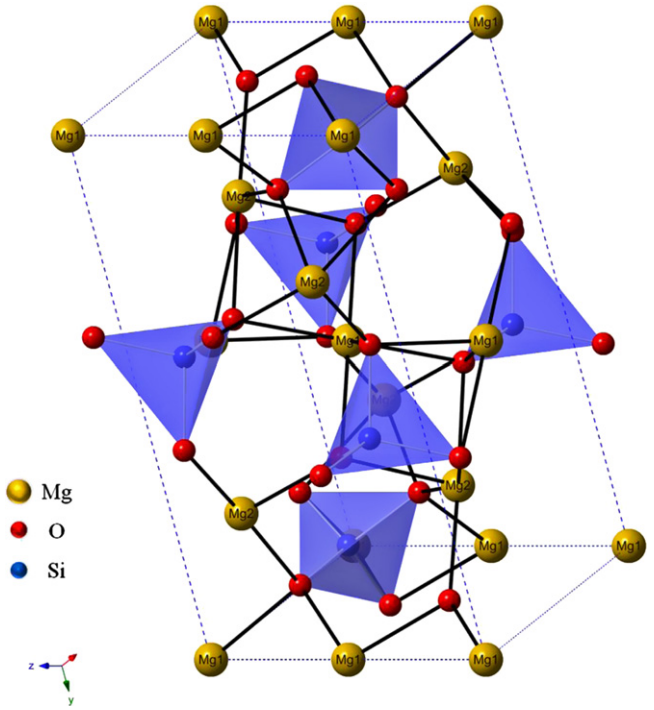

Fig. 1. View of the crystallographic structure of forsterite Mg_2SiO_4. Mg1 and Mg2 are Mg atoms in M1 and M2 sites respectively.

Because Fe^{2+} has a high spin state, it has a larger ionic radius than Mg^{2+}. Consequently, the M1 and M2 octahedra of fayalite are closer in structure than those of forsterite; while the volume difference between the two octahedra in fayalite is only half that of forsterite.

Among silicate minerals, olivines are susceptible to mechanical and chemical breakdown, with the common products of these reactions being serpentine phases [13]. Serpentinization is the most common form of olivine alteration, and can be considered in simple terms as the hydration of olivine. It is present in three forms: lizardite, antigorite and chrysotile (approximate composition: $Mg_3Si_2O_5(OH)_4$).

2.2. Material preparation

The olivine used in this study was mined at the Åheim Plant in Norway. It was sieved to obtain particle size ranging from 400 to 500 μm, and is referred to as natural olivine in this paper. When used as a catalyst, olivine was calcined at 1400 °C in air for 4 h which improve the mechanical properties for fluidized bed use [11].

2.3. Characterization

The chemical composition of olivine was obtained by Laser Ablation Inductively Coupled Plasma Mass Spectrometry (LA-ICP-MS) (CNRS—Institut de Recherches sur les Archéomatériaux, France).

Crystalline phases were determined by powder X-Ray Diffraction (XRD) on a Bruker D8 Advance diffractometer using a rotating copper anode (Cu-K_α) (λ = 1.5406 Å) operating at 40 kV and 40 mA in step scan mode with a step size of 0.016°.

Crystalline phases present at high temperature were determined by *in situ* High Temperature X-Ray Diffraction (HT-XRD) in air using a HTK16 Anton Paar chamber with ground sample deposited on a platinum ribbon heating stage.

The chemical and phase characterization were performed by Raman spectroscopy (InVia Reflex Renishaw) using a 633 nm laser wavelength at 13 mW (laser output). Individual spectra were collected under a microscope (100 × objective), with Raman-scattered light dispersed by a holographic grating of 1800 grooves/mm, and were detected by a charge coupled device (CCD) camera. Raman mappings were performed using two different objectives (× 20 and × 100) and a holographic grating of 600 grooves/mm.

3. Results and discussion

Table 1 lists the composition of the natural olivine and leads to a mean global formula of $(Mg_{0.92}Fe_{0.08})_2SiO_4$. It is

predominantly forsterite phase. Characterization of olivine phases was as follows:

3.1. Room temperature XRD crystalline phase determination

Fig. 2 illustrates the XRD data of both natural and calcined olivine at 1400 °C in the $2\theta = 10–50°$ range. As far as the natural olivine is concerned, the XRD data indicated the main diffraction lines were characteristic of the forsterite phase [Mg_2SiO_4]. Additional peaks were also present which corresponded to secondary crystalline phases such as enstatite [$MgSiO_3$], observed at $2\theta = 28.1°$ and 31.1°; serpentine [$Mg_3Si_2O_5(OH)_4$] observed at $2\theta = 12.5°$, 18.4° and 24.9°; and α-quartz [SiO_2] at $2\theta = 26.5°$.

Table 1
Elemental analysis of natural olivine.

	Si	Mg	Fe	Al	Ca	Cr	Mn	Ni	O[a]
mol%	15.43	23.04	1.98	0.23	0.04	0.10	0.03	0.11	59.04

[a]The value was obtained by subtraction.

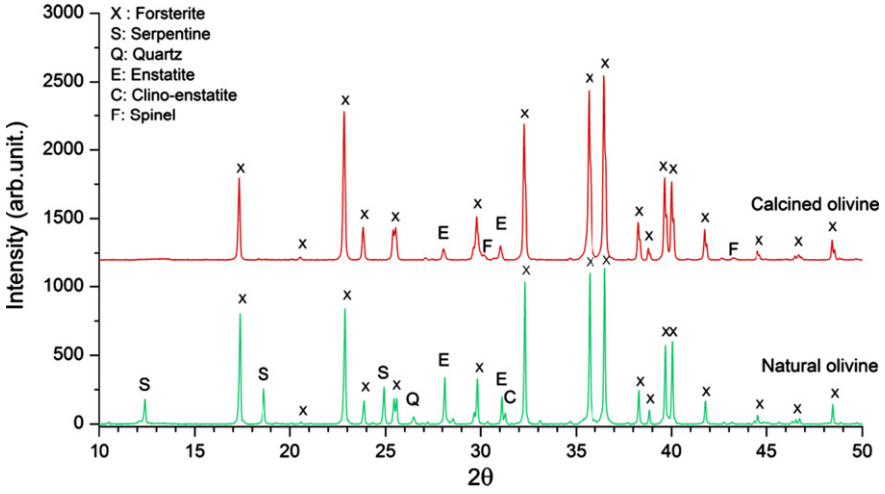

Fig. 2. X-ray diffractogram of the natural and calcined olivines.

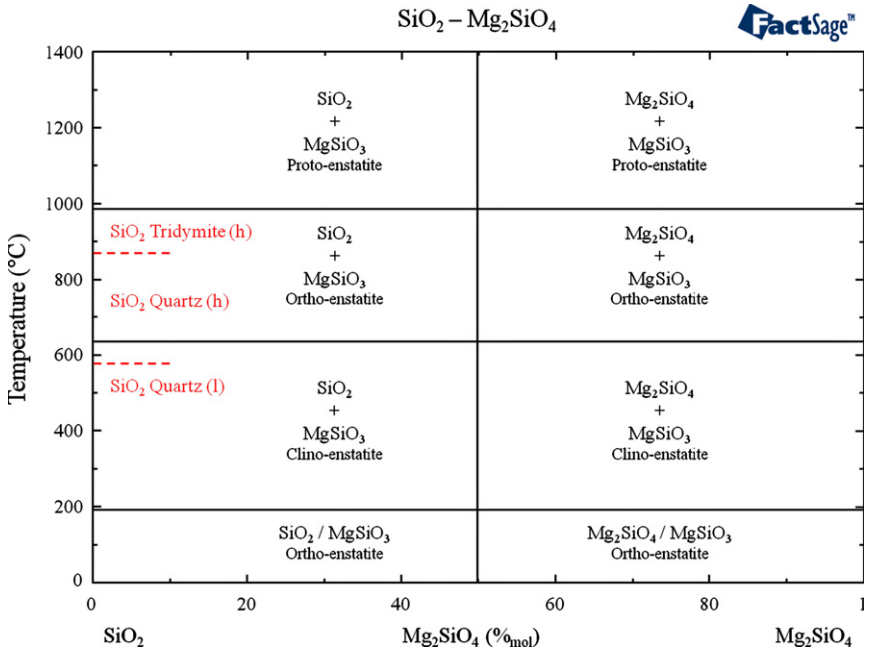

Fig. 3. Phase diagram of SiO_2–Mg_2SiO_4, $pO_2 = 0.2$ atm, FactSage v6.2.

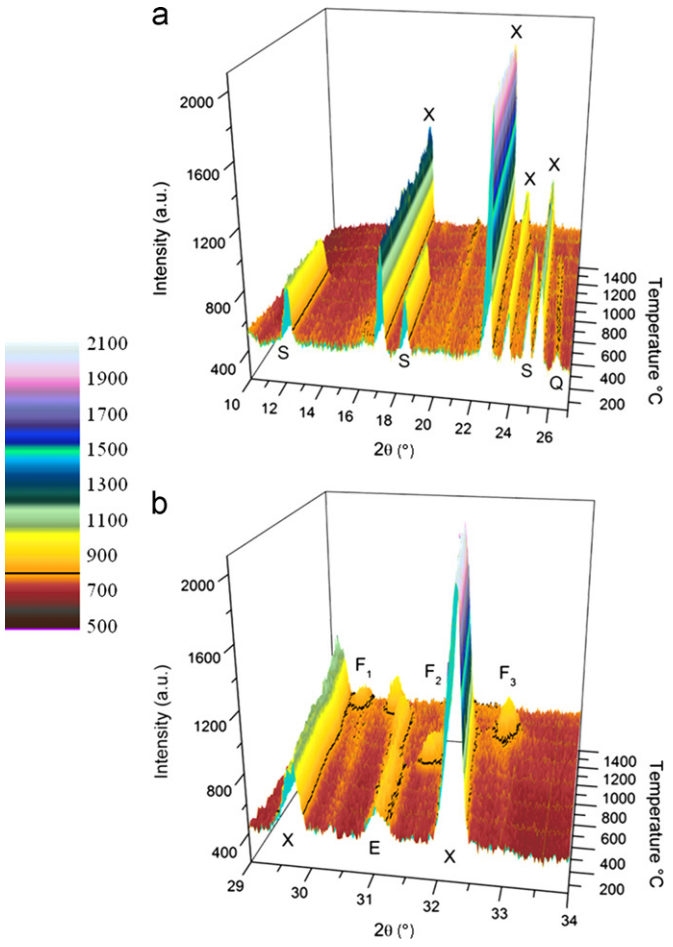

Fig. 4. *In situ* HT-XRD: (a) 2θ range 10—26°, X: Forsterite, S: Serpentine, Q: Quartz and (b) 2θ range 29–34°, E: Enstatite, F_1, F_2 and F_3: unidentified phases.

After calcination at 1400 °C, the hydrated serpentine phase [$Mg_3Si_2O_5(OH)_4$] and α-quartz SiO_2 completely disappeared and a new phase appears at $2\theta = 30.2°$ and 43.2°, which was attributed to a spinel phase. Based on the olivine material itself, numerous phases of iron oxide can appear after olivine calcination, including γ-Fe_2O_3, α-Fe_2O_3, Fe_3O_4 or $MgFe_2O_4$. However it is difficult to distinguish between these phases by X-ray diffraction [11].

It is noteworthy that for the sample calcined at 1400 °C, clino-enstatite changed into proto-enstatite, as confirmed by the thermodynamic calculation with FactSage software (Fig. 3). Chemical equilibrium model calculations used FactSage v6.2 with the FToxid database [14].

3.2. High temperature XRD crystalline phase determination

Fig. 4 illustrates the *in situ* HT-XRD data of olivine in the $2\theta = 10–26°$ and 29–34° ranges. The hydrated serpentine phase disappears at about 600 °C. Both forsterite and enstatite phases seem to be formed after the heat treatment of olivine in air according to the following chemical equation:

$$2Mg_3Si_2O_5(OH)_4 \rightarrow 2Mg_2SiO_4 + 2MgSiO_3 + 4H_2O \quad (1)$$

The resulting forsterite phase can then react with α-quartz [SiO_2], which is no longer present at about 1030 °C, following the reaction (Eq. (2)) forming a pyroxene phase such as enstatite [$MgSiO_3$] according to the thermodynamic diagram shown in Fig. 3.

$$Mg_2SiO_4 + SiO_2 \rightarrow 2MgSiO_3 \quad (2)$$

In situ HT-XRD of olivine in air (Fig. 4b) indicated new phases formed at F_1: ($2\theta = 29.7°$) between 1185 and

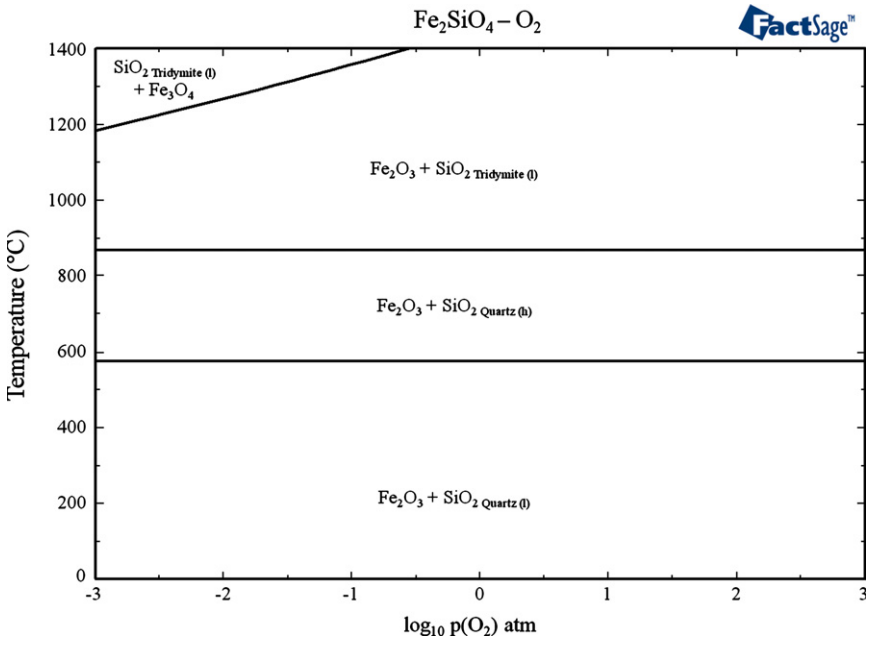

Fig. 5. Phase diagram of Fe_2SiO_4–O_2, FactSage v6.2.

1368 °C, F_2: ($2\theta = 31.5°$) between 590 and 780 °C and F_3: ($2\theta = 32.7°$) between 960 and 1200 °C. According to the literature, these phases could be either hematite [α-Fe_2O_3], magnetite [Fe_3O_4], or magnesioferrite [$MgFe_2O_4$] but also formed a solid solution such as $MgFe_2O_4$-Fe_3O_4 and/or $MgFe_2O_4$–α-Fe_2O_3 [11]. XRD was not able to determine the kind of iron oxide phases due to its peak resolution and peak overlapping of phases in olivine.

The phase transformation of clino-enstatite into ortho-enstatite was observed at 610 °C on *in situ* HT-XRD data, mainly at $2\theta = 31°$. Indeed, a phase change occurred at 1100 °C that could be attributed to a proto-enstatite phase. The phase diagram in Fig. 3 confirms the experimental transformations of enstatite observed at high temperature.

During the calcination process in air, olivine is known to oxidize at high temperatures. Magnetite/hematite phases are then produced from the oxidation of the fayalite phase according to the following reactions [15]:

$$3Fe_2SiO_4 + O_2 \rightarrow 2Fe_3O_4 + 3SiO_2 \quad (3)$$

$$2Fe_2SiO_4 + O_2 \rightarrow 2Fe_2O_3 + 2SiO_2 \quad (4)$$

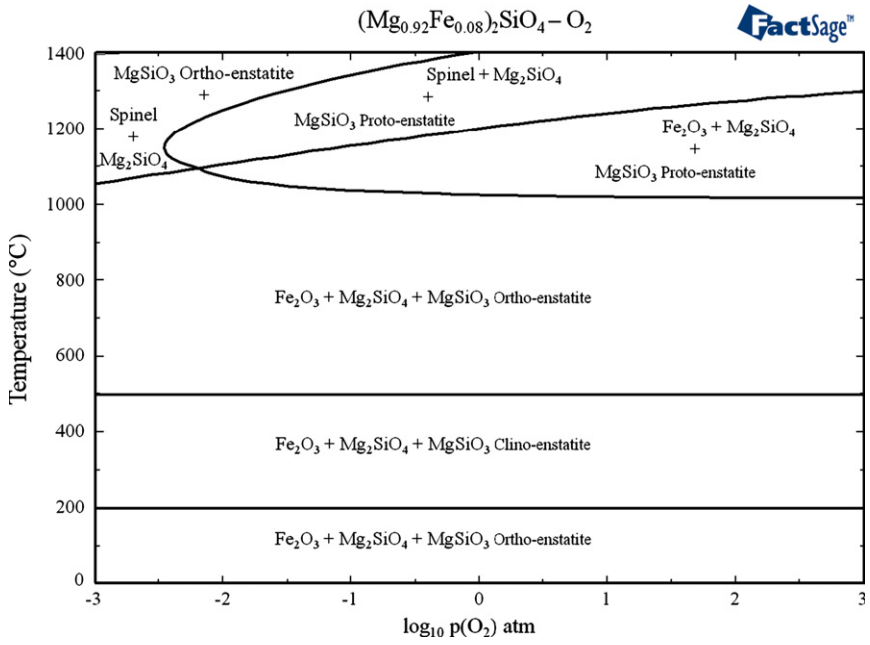

Fig. 6. Phase diagram of $(Mg_{0.92}Fe_{0.08})_2SiO_4$–$O_2$, FactSage v6.2.

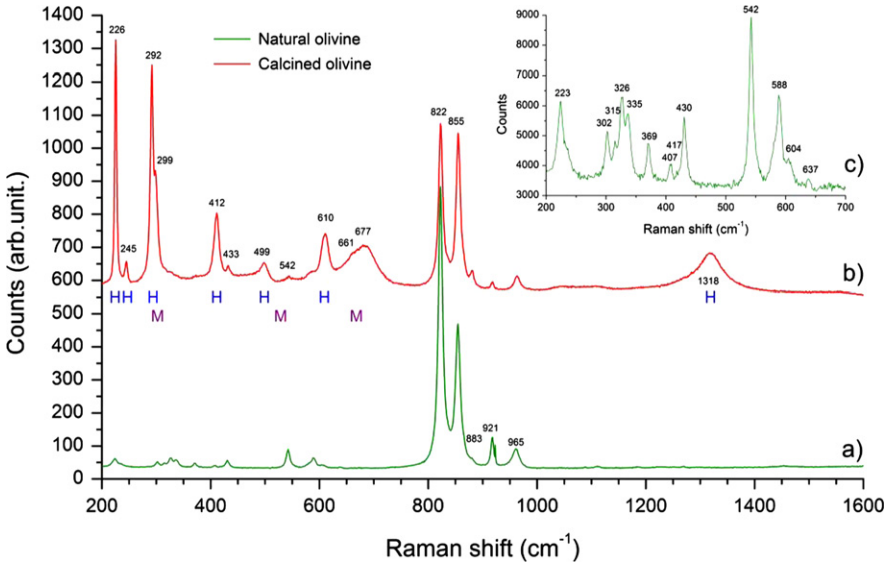

Fig. 7. Raman spectra of (a) natural olivine and (b) calcined olivine (H: Hematite and M: Magnetite). The inset (c) shows details of the low-wavenumber range of natural olivine.

Fig. 5 displays the phase diagram of Fe_2SiO_4–O_2. The phase diagram indicates that both magnetite and hematite phases are present at 1400 °C in air condition (log $p(O_2) = -0.70$ atm). The silica phase, that was observed, can also react with forsterite to form pyroxene phases (Eq. (2)).

Fig. 6 describes the phase diagram of $(Mg_{0.92}Fe_{0.08})_2SiO_4$–$O_2$. The result confirms the formation of forsterite [Mg_2SiO_4] and Proto-enstatite [$MgSiO_3$] above 1000 °C at an O_2 partial pressure of 0.2 atm [log $p(O_2) = -0.70$ atm]. Moreover, at equilibrium above 1165 °C, a spinel phase is formed with magnetite [Fe_3O_4] and magnesioferrite [$MgFe_2O_4$].

3.3. Raman spectroscopy phase analysis

The solid–solution crystal phases formed in olivine were investigated using Raman spectroscopy. According to group theory, 81 zone-centre optical phonon modes are predicted for the structural group of Mg_2SiO_4 but only 36 modes are Raman active. In the olivine used in this study, due to the random substitution of Mg/Fe in the cation site, group theory cannot rigorously be applied, and the number of resulting Raman allowed modes is necessarily higher. Fig. 7a displays the Raman spectrum of the natural olivine studied in the 200–1600 cm^{-1} wavenumber range. The observation of fewer bands than theoretically possible is due to the weak intensities of some bands and to the close positions of others. Basically, the Raman spectrum of olivine can be divided into two spectral regions: 400–700 cm^{-1} and 700–1100 cm^{-1}. The bands of the first spectral region result from internal bending vibrational modes of the SiO_4 ionic groups [16]. The second region is dominated by the internal stretching vibrational modes of the same group [16]. The most prominent features are the doublet bands appearing at 822 cm^{-1} and 855 cm^{-1},

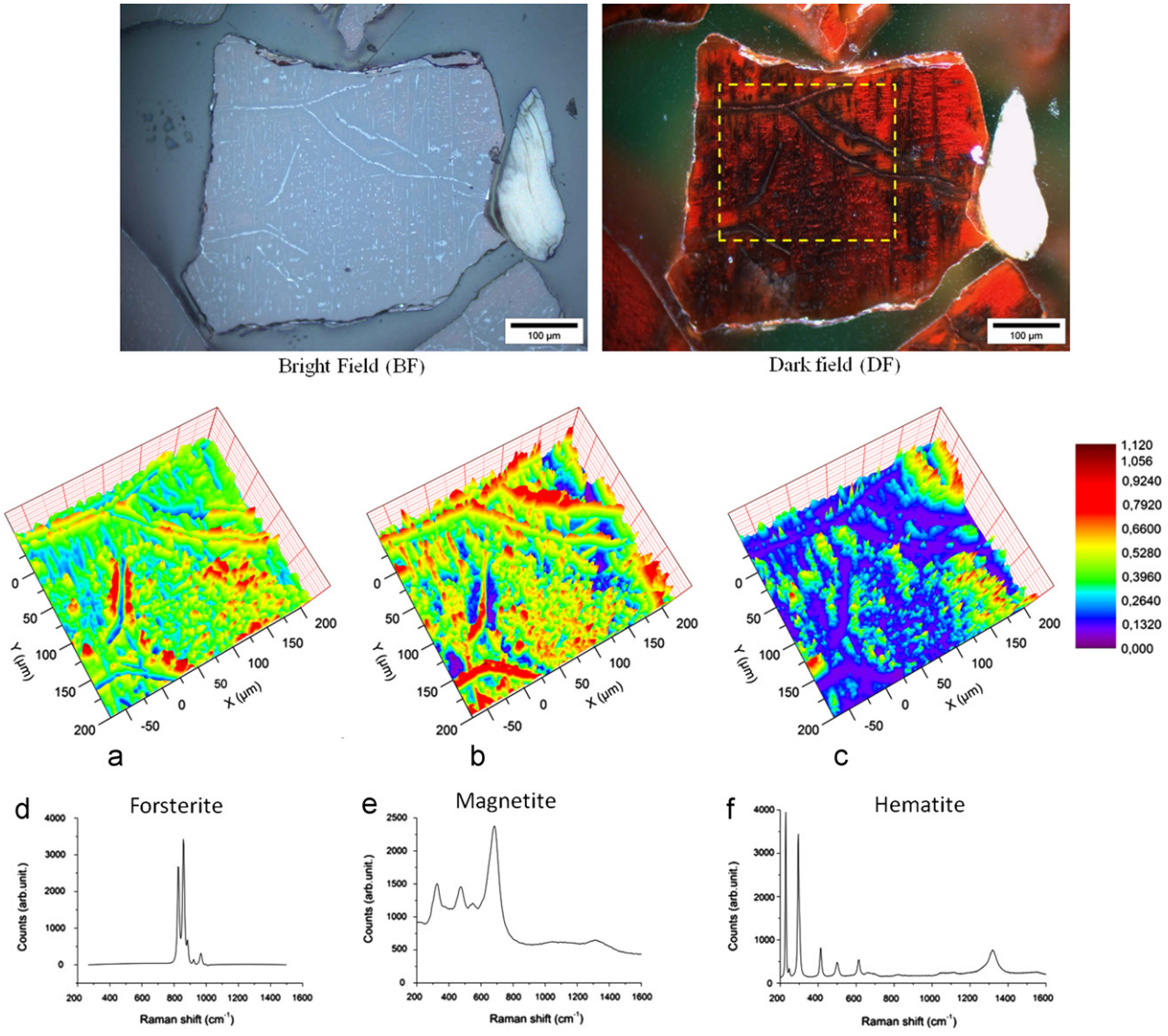

Fig. 8. Analyzed zone of calcined olivine at 1400 °C and Raman mapping: score maps of forsterite (a), magnetite (b) and hematite (c) with corresponding Raman components (d–f).

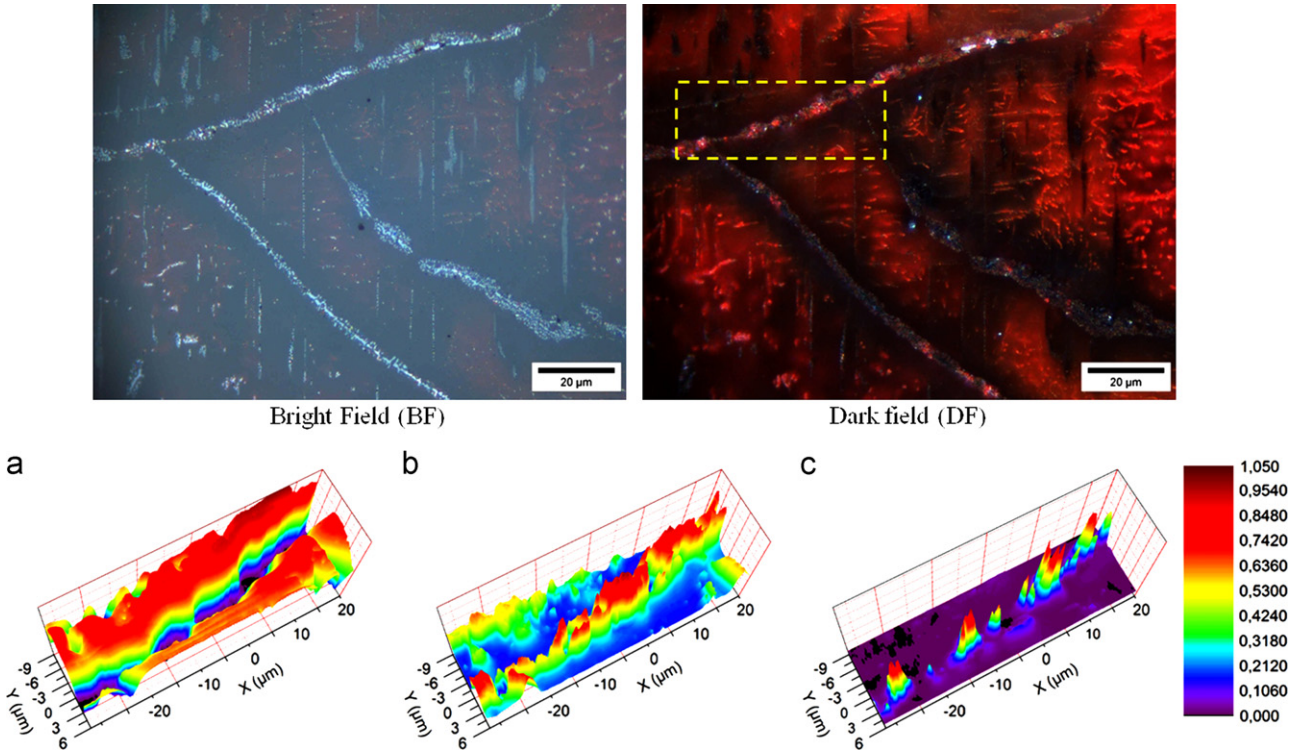

Fig. 9. Analyzed zone of calcined olivine at 1400 °C in Raman mapping in high special resolution: score maps of forsterite (a), magnetite (b) and hematite (c).

a doublet often considered as the signature of olivine. Other Raman features below 400 cm^{-1} are shown in the inset of Fig. 6c which are assigned to lattice modes: rotational and translational motions of SiO_4 as a unit, and translational motions of octahedral cations (Mg^{2+}, Fe^{2+}) in the crystal lattice [16–19].

On the other hand, Fig. 7b displays Raman spectrum of the calcined olivine at 1400 °C for 4 h in the 200–1600 cm^{-1} wavenumber range. The spectrum indicates significant changes in the 200–700 cm^{-1} wavenumber range. These changes are due to the iron alteration into oxide forms such as hematite (corresponding bands are located at 226, 245, 292, 412, 499, 610 and 1318 cm^{-1}) and magnetite (corresponding bands are located at 299, 532 and 677 cm^{-1}) [20,21]. In these spectra, care was taken to avoid heating induced by the Raman laser, as underlined by El Mendili et al. [21]. But in the present case, the iron oxides were less sensitive to heating than maghemite [γ-Fe_2O_3].

Fig. 8 presents the reflected light micrograph obtained by both dark and bright field modes on the calcined olivine at 1400 °C. A simple visual inspection of these images shows a heterogeneous structure, composed of dark and bright areas. The dark areas appear in the form of veins on the polished grain surface. Consequently Raman mapping appears to be a well-suited technique to investigate the distribution of the resulting phases and components. Spectra are sequentially collected, point by point, over a defined region (dashed square in the micrograph), with a $\times 20$ objective, and a separation between neighbor points of 1.6 µm. Due to the considerable number of spectra obtained (25,670 spectra), a first data processing by Principal Component Analysis (Renishaw Wire 3.3 software) was performed, giving an indication of three independent components in the map, with characteristic features of forsterite, magnetite and hematite. Then, a Direct Classical Least squares (DCLS) method was used. It consisted of reconstructing the map by a linear combination of spectra from the three pure components contained in the sample.

Fig. 8(a–c) displays the map scores of each of the three constituents ((a) Forsterite, (b) magnetite and (c) hematite), with the individual spectral components as shown in Fig. 8(d–f), taken at specific points of the map where each of them were concentrated. In particular, the magnetite phase appears to be mainly concentrated in the dark regions and inside the veins, whereas the hematite phase seems to be located in small amounts, in the bright regions.

Fig. 9 exhibits Raman mapping, with higher spatial resolution ($\times 100$ objective, step between neighbor points of 0.2 µm), performed on a small region encompassing a distinguishable vein. The same DCLS process as before was applied. The map scores of each component show that the vein also contains a small amount of hematite phase, which was interposed between magnetite phase zones. The vein was with magnetite and hematite interposed and was determined to be 86% magnetite and 14% hematite, with forsterite coating the vein. In regard to all these observations, Raman mapping spectroscopy was found to make identification of olivine alteration and phase transformations *vs.* temperature easier than other analytical tools.

4. Conclusion

In summary, we have reported here on the characterization of the phase transformations of olivine at varying temperatures up to 1400 °C in air. Natural olivine was not an inert silicate, its initial composition $(Mg_{0.92},Fe_{0.08})_2SiO_4$ transformed by thermal decomposition at high temperature by dehydration and oxidation of fayalite. XRD analysis highlighted the structural transformations consisting of the dehydration of serpentine below 600 °C, the disappearance of the quartz phase at 1030 °C, and the formation of iron oxide phases. These results were in good agreements with the thermochemical analysis. Iron oxide phases were successfully identified by Raman spectroscopy which appears to be a complementary method to XRD. Hematite and magnetite phases have shown to be heterogeneously distributed within olivine material as assessed by Raman mapping. The resulting phase transformations provide a catalytic property to olivine material for BFB reactor.

Acknowledgments

We thank the ANR (Agence Nationale de la Recherche) for funding the GAMECO project focused on improving gasification for Combined Heat and Power (CHP) applications.

We thank Guy Matzen and Emmanuel Véron from CEMHTI team "Oxide glasses: glass forming, crystallization" for the *in situ* HT-XRD.

References

[1] S. Rapagna, N. Jand, A. Kiennemann, P.U. Foscolo, Steam-gasification of biomass in a fluidised-bed of olivine particles, Biomass and Bioenergy 19 (2000) 187–197.

[2] P. Basu, Biomass gasification and pyrolysis, 1st edition, in: Practical Design and Theory, Academic Press Elsevier, Burlington, USA, 2010 (Chapter 6: Design of biomass gasifiers). ISBN: 978-0-12-374988-8.

[3] M. Bartels, J. Nijenhuis, J. Lensselink, M. Siedlecki, W. de Jong, F. Kapteijn, et al., Detecting and counteracting agglomeration in fluidized bed biomass combustion, Energy and Fuels 23 (2009) 157–169.

[4] M. Öhman, A. Nordin, B.-J. Skrifvars, R. Backman, M. Hupa, Bed agglomeration characteristics during fluidized bed combustion of biomass fuels, Energy and Fuels 14 (2000) 169–178.

[5] T. Liliedahl, K. Sjöström, K. Engvall, C. Rosén, Defluidisation of fluidised beds during gasification of biomass, Biomass and Bioenergy 35 (2011) S63–S70.

[6] S. Li, L. Shang, H. Teng, Q. Lu, A model for agglomeration in biofuel fired fluidized bed, Journal of Thermal Science 19 (2010) 451–458.

[7] G. Olofsson, Z. Ye, I. Bjerle, A. Andersson, Bed agglomeration problems in fluidized-bed biomass combustion, Industrial and Engineering Chemistry Research 41 (2002) 2888–2894.

[8] J.S. Heaton, R.C. Engstrom, *In situ* atomic force microscopy study of the differential dissolution of fayalite and magnetite, Environmental Science and Technology 28 (1994) 1747–1754.

[9] L.E. Mayhew, S.M. Webb, A.S. Templeton, Microscale imaging and identification of Fe speciation and distribution during fluid–mineral reactions under highly reducing conditions, Environmental Science and Technology 45 (2011) 4468–4474.

[10] D. Swierczynski, C. Courson, L. Bedel, A. Kiennemann, J. Guille, Characterization of Ni–Fe/MgO/olivine catalyst for fluidized bed steam gasification of biomass, Chemistry of Materials 18 (2006) 4025–4032.

[11] D. Swierczynski, C. Courson, L. Bedel, A. Kiennemann, S. Vilminot, Oxidation reduction behavior of iron-bearing olivines $(Fe_x\,Mg_{1-x})_2SiO_4$ used as catalysts for biomass gasification, Chemistry of Materials 18 (2006) 897–905.

[12] W.A. Deer, R.A. Howie, J. Zussman, An Introduction to the Rock-Forming Minerals, 2nd ed., Longman Scientific and Technical, 1992.

[13] V.E. Hamilton, Thermal infrared (vibrational) spectroscopy of Mg–Fe olivines: a review and applications to determining the composition of planetary surfaces, Chemie Der Erde—Geochemistry 70 (2010) 7–33.

[14] C.W. Bale, E. Bélisle, P. Chartrand, S.A. Decterov, G. Eriksson, K. Hack, et al., FactSage thermochemical software and databases—recent developments, Calphad 33 (2009) 295–311.

[15] S.-L. Hwang, T.-F. Yui, H.-T. Chu, P. Shen, Y. Iizuka, H.-Y. Yang, et al., Hematite and magnetite precipitates in olivine from the Sulu peridotite: a result of dehydrogenation–oxidation reaction of mantle olivine? American Mineralogist 93 (2008) 1051–1060.

[16] K.E. Kuebler, B.L. Jolliff, A. Wang, L.A. Haskin, Extracting olivine (Fo–Fa) compositions from Raman spectral peak positions, Geochimica Et Cosmochimica Acta 70 (2006) 6201–6222.

[17] B.A. Kolesov, C.A. Geiger, A Raman spectroscopic study of Fe–Mg olivines, Physics and Chemistry of Minerals 31 (2004) 142–154.

[18] B.A. Kolesov, J.V. Tanskaya, Raman spectra and cation distribution in the lattice of olivines, Materials Research Bulletin 31 (1996) 1035–1044.

[19] A. Chopelas, Single crystal Raman spectra of forsterite, fayalite, and monticellite, American Mineralogist 76 (1991) 1101–1109.

[20] D.L.A. de Faria, S.V. Silva, M.T. de Oliveira, Raman microspectroscopy of some iron oxides and oxyhydroxides, Journal of Raman Spectroscopy 28 (1997) 873–878.

[21] Y. El Mendili, J.-F. Bardeau, N. Randrianantoandro, A. Gourbil J.-M. Greneche, A.-M. Mercier, et al., New evidences of *in situ* laser irradiation effects on γ-Fe_2O_3 nanoparticles: a Raman spectroscopic study, Journal of Raman Spectroscopy 42 (2011) 239–242.